APPLIED SCIENCES AND ENGINEERING

Electrically driven monolithic subwavelength plasmonic interconnect circuits

Yang Liu,[1,2] Jiasen Zhang,[3,4]* Huaping Liu,[4,5] Sheng Wang,[2] Lian-Mao Peng[1,2]*

In the post-Moore era, an electrically driven monolithic optoelectronic integrated circuit (OEIC) fabricated from a single material is pursued globally to enable the construction of wafer-scale compact computing systems with powerful processing capabilities and low-power consumption. We report a monolithic plasmonic interconnect circuit (PIC) consisting of a photovoltaic (PV) cascading detector, Au-strip waveguides, and electrically driven surface plasmon polariton (SPP) sources. These components are fabricated from carbon nanotubes (CNTs) via a CMOS (complementary metal-oxide semiconductor)–compatible doping-free technique in the same feature size, which can be reduced to deep-subwavelength scale (~λ/7 to λ/95, λ = 1340 nm) compared with the 14-nm technique node. An OEIC could potentially be configured as a repeater for data transport because of its "photovoltaic" operation mode to transform SPP energy directly into electricity to drive subsequent electronic circuits. Moreover, chip-scale throughput capability has also been demonstrated by fabricating a 20 × 20 PIC array on a 10 mm × 10 mm wafer. Tailoring photonics for monolithic integration with electronics beyond the diffraction limit opens a new era of chip-level nanoscale electronic-photonic systems, introducing a new path to innovate toward much faster, smaller, and cheaper computing frameworks.

INTRODUCTION

On-chip electrically driven miniaturized optoelectronic integrated circuits (OEICs) that combine the high bandwidth of a photonic network with the compactness of an electronic circuit are actively pursued in the post-Moore era to realize rapid data transmission and powerful signal processing (*1*, *2*). Therefore, considerable research efforts over the past several decades have been devoted to fabricating OEICs with silicon, germanium, II-VI and III-V semiconductors, nanowires, and an expanding class of two-dimensional (2D) materials (*3*–*9*). Nevertheless, none of these approaches have been demonstrated at the complete circuit level to enable photonics to monolithically interface with electronics with the same feature size. Currently, this gap between photonics and electronics can be bridged through plasmonics, which combines matter excitation and light fields, enabling the control of electromagnetic fields at the interface of a metal and a dielectric to overcome the diffraction limit (*10*–*13*). A wide range of plasmonic building blocks have been created to construct complete plasmonic circuits over the past few decades, including waveguides, antennas, splitters, modulators, surface plasmon polariton (SPP) sources, and detectors (*11*, *14*–*24*). However, a monolithic plasmonic interconnect circuit (PIC) has yet to be realized because of fabrication and material conflicts (*10*–*13*). In this regard, semiconducting single-walled carbon nanotubes (CNTs) provide a novel material platform for integrated nanoelectronics and optoelectronics because of their excellent properties, which include a direct bandgap, ballistic transportation, broadband response, and an ultrathin body of 1 to 3 nm (*25*, *26*). These features enabled considerable development of CNT electronics and optoelectronics, including p- and n-type transistors, electrically driven light-emitting diodes, photovoltaic (PV) detectors, and functional integrated circuits at a primitive system level (*25*–*36*).

Here, we demonstrate that an energy-efficient SPP source, PV detector, and Au-strip waveguide can realize monolithic electrically driven PICs. These features are fabricated from CNTs at a subwavelength scale via complementary metal-oxide semiconductor (CMOS)–compatible, doping-free techniques. This approach enables chip-level throughput capability for potential applications, such as data transport repeaters, in modern computing systems.

RESULTS

Structure and principle of the PIC

Figure 1 shows a schematic of the electrically driven PIC system consisting of two SPP sources, two Au-strip waveguides, and a two-cell PV cascading detector on a typical silicon wafer. In the SPP sources (channel length L = 0.5 μm; channel width W = 10 μm; illustrated in section S1 and fig. S1), chirality-selected (8, 4) and (8, 3) CNTs (detailed characterization results are presented in section S2, fig. S2, and table S1) are in contact with Ti/Au electrodes. The cascading detector is composed of high–semiconducting purity CNTs (specific characterization in section S2, fig. S2, and table S1), which are in contact with Pd/Sc electrodes (*28*). The channel length and width of the detector (fig. S1) are 1 and 10 μm, respectively, if without special illustration. All SPP sources and detectors are covered with a 20-nm HfO_2 layer as both an electrically insulating layer and a metal-dielectric interface for SPP generation and detection. Finally, the Au-strip waveguides (thickness t = 80 nm; width, 500 or 200 nm; length, 1 to 10 μm) are fabricated on top of the HfO_2 layer to optically connect the sources to the detector.

Plasmonic interconnection is a multistep process consisting of SPP generation, propagation, and near-field detection. First, the energy released from the (8, 4) and (8, 3) CNTs is directly converted into an SPP mode via near-field coupling, which can be transported away by the Au-strip waveguides. The intensity distribution of the plasmonic waveguide mode for a 500-nm-wide Au strip (Fig. 1, inset) shows that the field is tightly confined below the Au strip because of the asymmetric refractive index distribution (more analyses are given in section S3 and fig. S3) (*14*). Then, the SPPs propagate along the waveguides and are absorbed by the CNTs in the PV cascading detector. The source is electrically driven in the PIC system, and the energy propagation from the

[1]Key Laboratory for the Physics and Chemistry of Nanodevices and Academy for Advanced Interdisciplinary Studies, Peking University, Beijing 100871, China. [2]Key Laboratory for the Physics and Chemistry of Nanodevices and Department of Electronics, Peking University, Beijing 100871, China. [3]State Key Laboratory for Mesoscopic Physics and Department of Physics, Peking University, Beijing 100871, China. [4]Collaborative Innovation Center of Quantum Matter, Beijing 100871, China. [5]Beijing National Laboratory for Condensed Matter Physics, Institute of Physics, Chinese Academy of Sciences, Beijing 100190, China.
*Corresponding author. Email: jszhang@pku.edu.cn (J.Z.); lmpeng@pku.edu.cn (L.-M.P.)

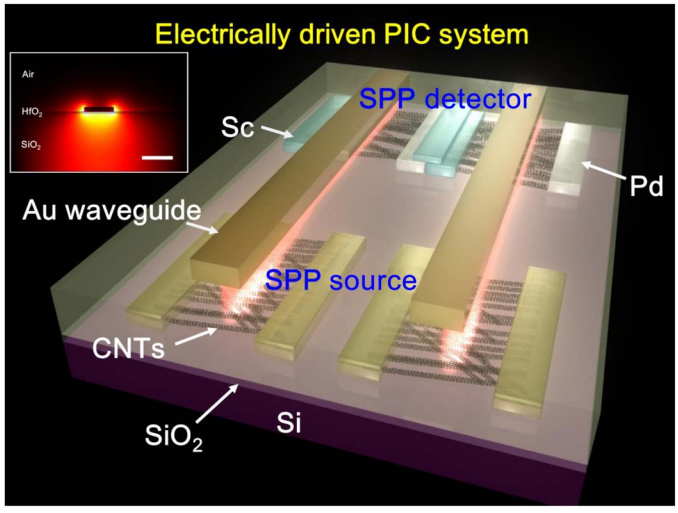

Fig. 1. Electrically driven PIC system based on CNTs. The inset shows the mode distribution of a 500-nm-wide Au-strip waveguide. Scale bar, 500 nm.

source to the detector is conducted by SPPs for direct transformation into electricity through the PV cascading detector without any far-field optical processes. Therefore, this is a "dark-state" PIC system in the connection plane (*24*).

Far-field characteristics of the CNT SPP source

Here, we illustrate the far-field electroluminescence (EL) characteristics of the CNT emitters and SPP sources measured with an external spectrometer. In practice, five emission channels (Fig. 2A) were constructed to increase the coupled SPP intensity. The typical output characteristics of the CNT emitters are shown in Fig. 2B with a source-drain current of ~1.63 mA at V_{ds} = −8 V. The corresponding EL spectrum (Fig. 2C) is attributed to the emission from the (8, 4) and (8, 3) CNTs via Lorentzian fitting at 0.92 and 1.03 eV with full width at half maximum (FWHM) of ~121 and ~135 meV, respectively. The emission peak widths of the (8, 4) and (8, 3) CNTs are substantially narrower than those of nonchirality-selected CNTs (fig. S4). The emission intensity follows an exponential relationship versus the voltage bias (Fig. 2D; see also inset), indicating an impact-excitation–dominated EL process (*35*, *36*). Compared with the photoluminescence (PL) spectra (fig. S5), the EL spectra of the (8, 4) and (8, 3) CNTs are red-shifted by ~172 and ~252 meV, respectively, indicating "trion"-dominated infrared (IR) emission (*36*). The trion mechanism lightens the otherwise "dark" excitons and pushes the emission band toward the telecommunication wavelength of ~1310 nm, which greatly reduces the propagation loss compared with the visible band (for example, 600 nm; fig. S6).

Because the SPP dispersion curve is to the right of the light line of the dielectric, coupling between the light and SPPs usually requires gratings or prisms for phase matching (*10*–*13*). Alternatively, the near-field CNTs act as point sources for near-field excitation of the SPPs propagating along the Au strip (Fig. 2E) (*21*, *37*), which is desirable to construct a highly compact PIC. Specifically, the photonic mode of the waveguide is cut off, and the CNTs decay mainly through coupling to the SPP modes in the near field, that is, the propagating mode (SPPs) along the waveguide and the standing wave polarized perpendicularly to the Au strip [localized surface plasmons (LSPs)].

As evident in Fig. 2F, the output characteristic is basically unchanged before and after the Au strip was integrated. However, the FWHM of the EL spectrum (Fig. 2G) becomes narrower compared with that of the CNT emitter (Fig. 2C) because of the moderate Q-factor of the plasmonic mode (more detailed discussions are presented in section S7). The prominent IR emission (Fig. 2, G and H, inset) is due to the fact that LSPs are scattered into free space at the edges of the Au-strip waveguide (more analyses are given in section S8 and fig. S7); the integrated intensity also increases exponentially with increasing stimulated bias (Fig. 2H). Furthermore, the threshold voltage for IR emission of CNTs is ~1.2 V (*36*), which is approximately one order of magnitude lower than that reported previously (*22*), making the CNT SPP sources compatible with state-of-the-art electronic processing circuits. Therefore, this CNT-based SPP source is desirable to realize a monolithic, compact PIC configuration because of its directly coupled characteristic in the telecommunication band.

Far-field characteristics of the cascading CNT SPP detector

We combined contact engineering with high–semiconducting purity CNTs to construct a cascading barrier-free bipolar diode, which could be integrated with the Au-strip waveguide as a monolithic SPP detector. All the optoelectronic performance characteristics shown in Fig. 3 were measured under far-field incident IR illumination (λ = 1800 nm; schematically shown in Fig. 3B, inset).

We first characterized the bare CNT cascading detector (fig. S8A). It exhibited typical rectification and ambipolar transport characteristics in the dark (fig. S8B; see also inset) and demonstrated typical PV behavior with a logarithmical relationship of photovoltage as a function of the IR power density (fig. S8, C and D) (*3*). By integrating five Au-strip waveguides, we fabricated an actual five-cell cascading SPP detector (L = 0.5 μm, W = 10 μm), as shown in Fig. 3A (more detailed discussions of the cascading SPP detector are presented in section S10 and fig. S9). The rectification and ambipolar transport characteristics shown in Fig. 3 (B and C) were maintained after integration of the Au-strip waveguides, indicating that the waveguides did not introduce any obvious side effects. The photovoltage of the SPP cascading detector was 0.73 V under an incident power density of 5.78 W cm^{-2} (Fig. 3, D and E), which is attributed to the near-field enhancement of the Au-strip waveguide, as shown in fig. S10 (more detailed discussions are presented in section S11). The photovoltage of the SPP detector also follows a quasi-logarithmic relationship as a function of the incident power intensity (Fig. 3E), ensuring that it could also serve as a PV diode in the PIC system (*3*).

The most important figures of merit for characterizing detectors are the responsivity and the noise characteristics of the detector (*3*, *38*). The photovoltage responsivity of the CNT cascading detector is as high as 10^7 V/W in the telecommunication band, as previously discussed (*28*), which is sufficiently sensitive for the efficient detection of SPPs. In addition, the noise limit of the detector is the critical factor for the minimal energy per bit of OEICs. The power consumption can be significantly reduced by decreasing the noise level (*11*). As shown in Fig. 3F, the current noise characteristics of the cascading detector were measured both in PV mode with zero bias and under voltage-biased conditions. In the case of reverse bias, the noise decreased with increasing frequency, indicating 1/f noise-dominated behavior (*3*). By contrast, Johnson noise was dominant in the PV operation mode indicated as a flat noise spectrum with a specific noise level of 3.45 $fA/Hz^{1/2}$ at f = 1 Hz, which is very close to the theoretical limit. In principle, the energy consumption of the detector might be ultimately reduced to 4 k_BT (where k_B is the Boltzmann constant and T is the operating temperature), which is four orders of magnitude lower than the current light-level standards of 100,000 k_BT (*11*). Therefore, this highly sensitive, low-power, miniature

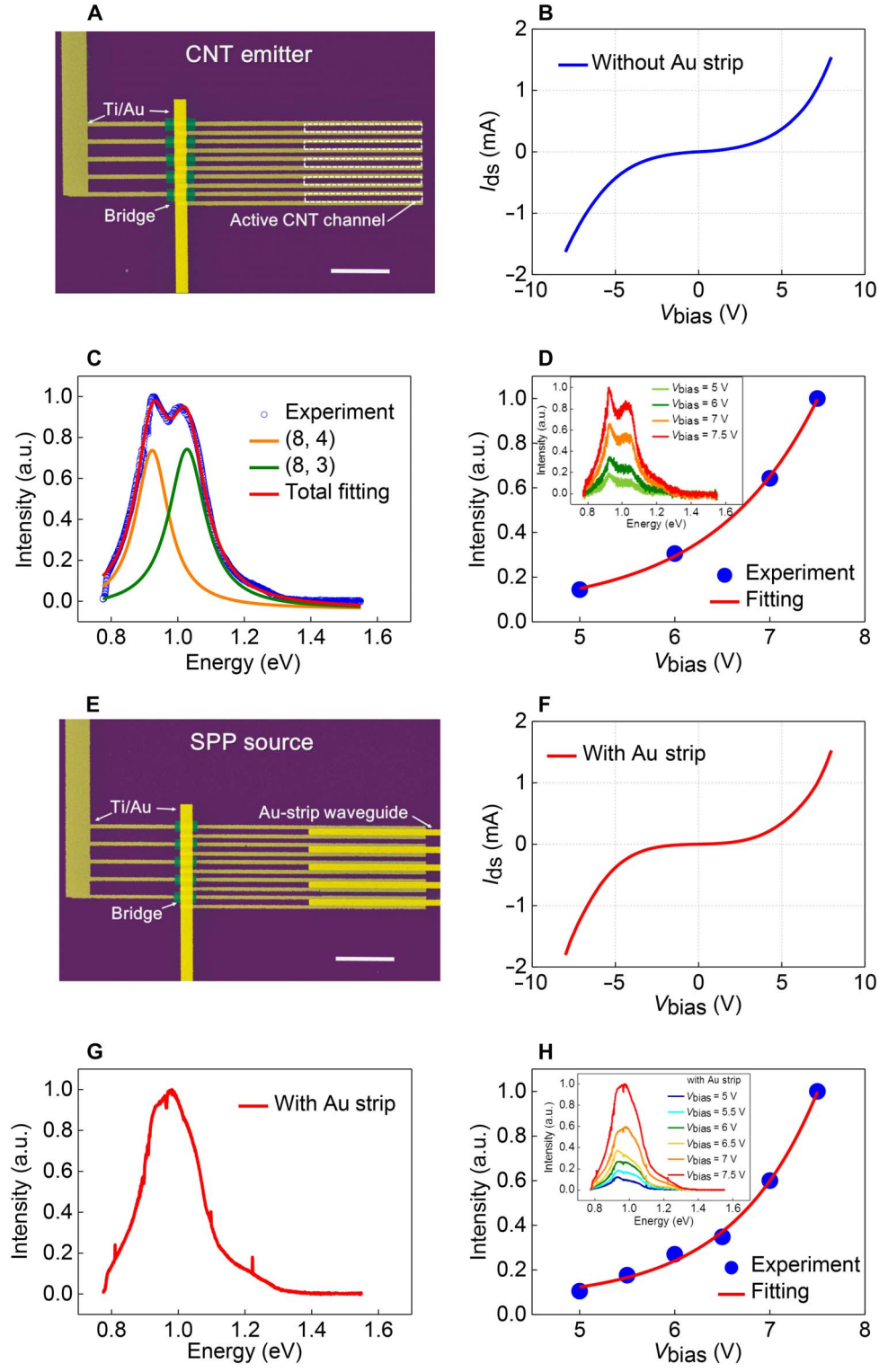

Fig. 2. On-chip CNT-based emitters and SPP sources. (**A**) False-color SEM image of the practical five-channel CNT emitters. Scale bar, 5 μm. (**B**) Output characteristics of the CNT emitters. (**C**) EL spectrum of the CNT emitters and its Lorentzian fitting. a.u., arbitrary units. (**D**) Integrated EL emission intensity versus voltage bias. Inset: EL spectra of CNT emitters under different voltage biases. (**E**) False-color SEM image of the practical five-channel CNT SPP sources. Scale bar, 5 μm. (**F**) Output characteristics of SPP sources. (**G**) EL spectrum of the SPP sources. (**H**) Integrated EL emission intensity versus voltage bias. Inset: Corresponding EL spectra under different voltage biases.

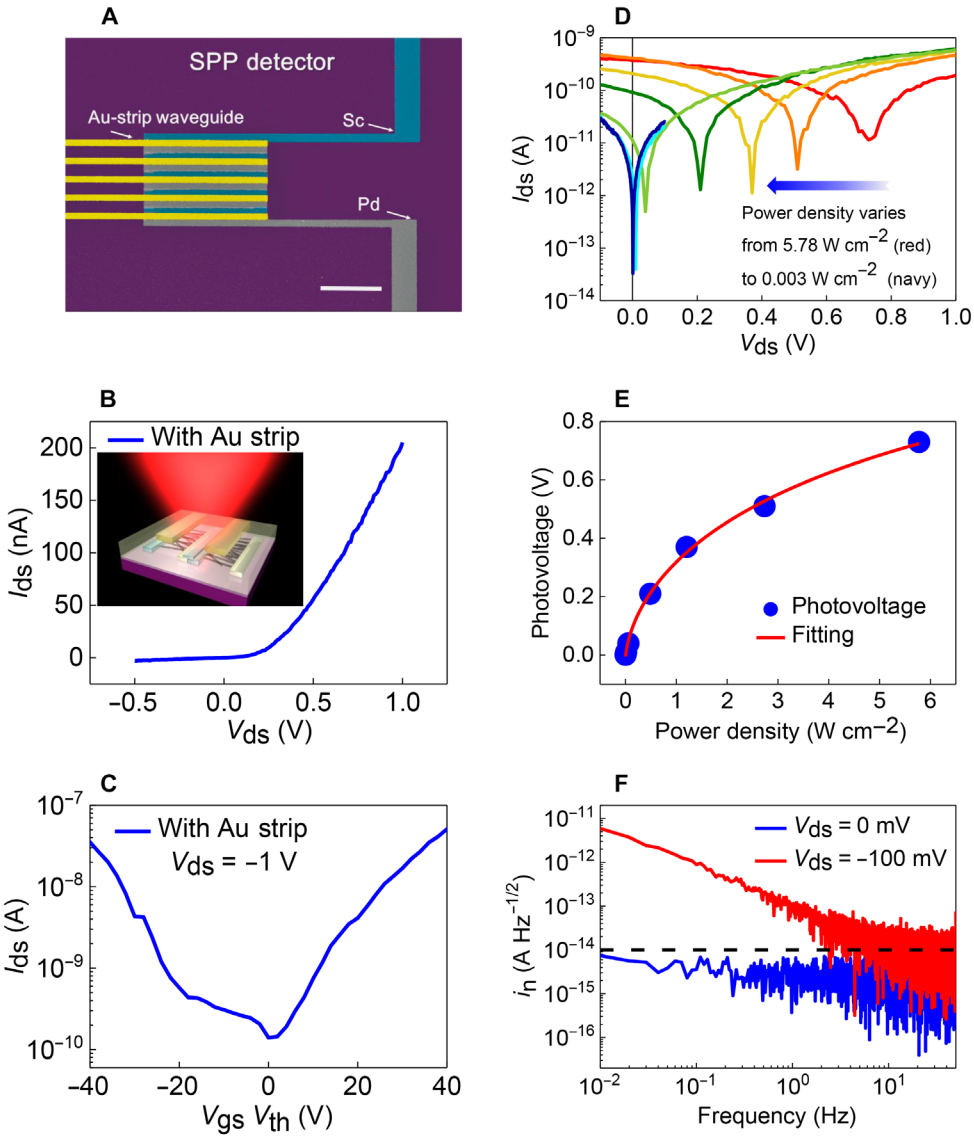

Fig. 3. Monolithic CNT PV cascading SPP detector. (**A**) False-color SEM image of the practical five-cell cascading SPP detector. Scale bar, 5 μm. (**B**) Output characteristics of the detector. Inset: Schematic of the detector under incident IR illumination. (**C**) Transfer characteristics of the detector with V_{ds} = −1 V. (**D**) Output characteristics of the SPP detector under different illumination intensities. (**E** and **F**) PV behavior (E) and noise spectra (F) of the SPP detector.

PV cascading detector is a desirable component to construct large-scale, compact PIC systems.

Near-field propagation characteristics of the electrically driven PIC system

Unlike the schematic in Fig. 1, the real PIC system is somewhat complex. To increase the coupled signal intensity of the source and signal-to-noise ratio of the detector, the PIC system involves five communication channels: five SPP sources, five Au-strip waveguides, and a five-cell cascading SPP detector. On top of each communication channel is an Au-strip waveguide, which is simultaneously part of the source, detector, and transmission line. We fabricated systems 1 (S1), 2 (S2), and 3 (S3) with different waveguide lengths of 1, 5, and 10 μm, respectively, as illustrated in Fig. 4 (A to C).

The diameters of the CNTs used in the PIC were less than 2 nm (table S1), locating them in the near-field region without introducing strong scattering centers to the Au-strip waveguides. Thus, the energy released by the (8, 4) and (8, 3) CNTs in the source can be coupled in the near-field region and propagate at the bottom surface of the Au-strip waveguide toward the detector end. 3D finite-difference time-domain (FDTD) simulations provide further insights into the propagation process (Fig. 4D; additional analyses are given in section S12). Finally, the propagating SPP energy is directly absorbed and converted into electrical signals by the near-field PV cascading detector.

When a bias (V_{bias} = 7 V) was applied to the S1, S2, and S3 sources, typical short-circuit current (I_{plas}) and open-circuit voltage (photovoltage) were generated, as shown in Fig. 4E; both the I_{plas} and the photovoltage decreased with increasing propagation

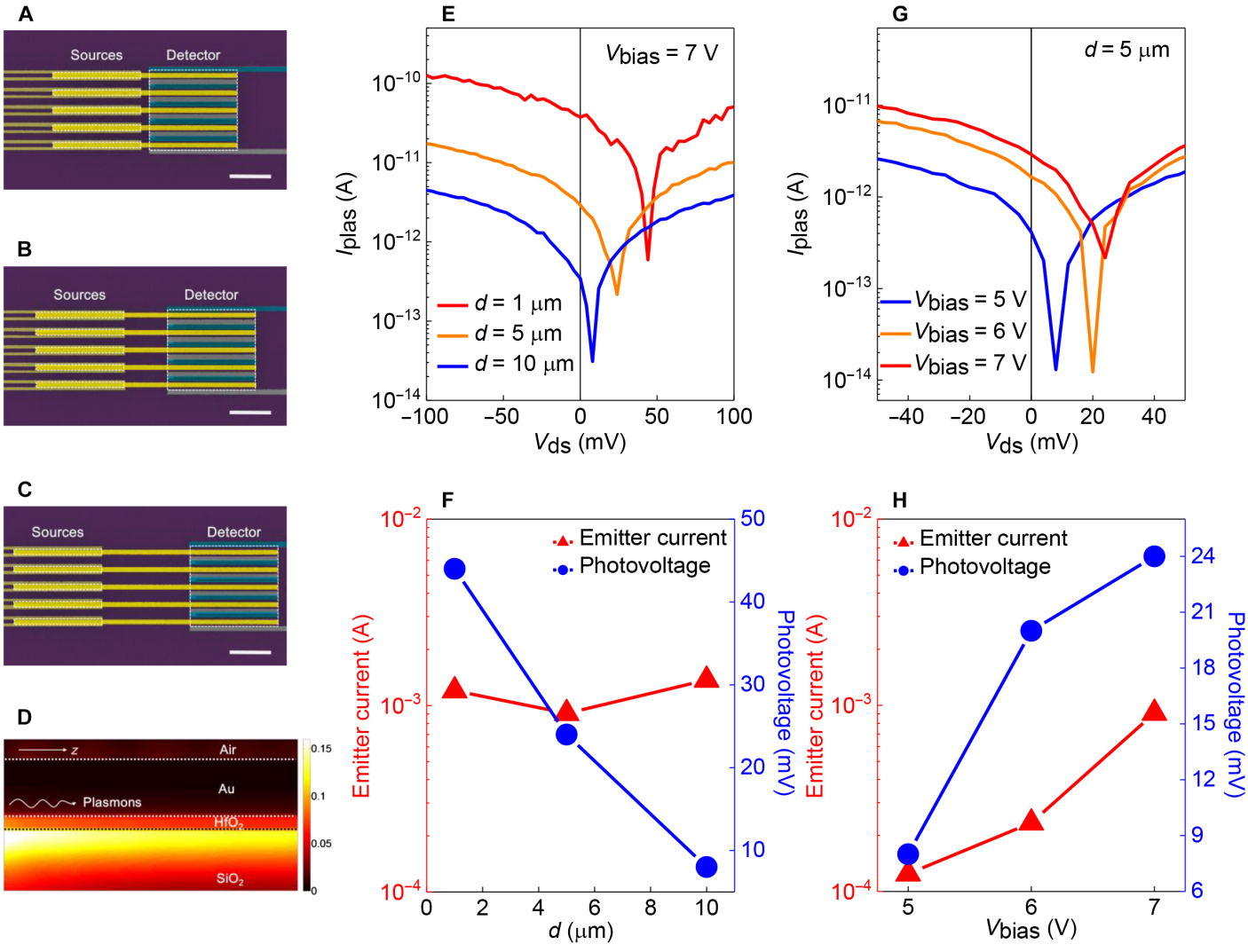

Fig. 4. Characteristics of the electrically driven PIC system. (**A** to **C**) SEM images of the PICs with different propagation lengths: d = 1 μm (A), 5 μm (B), and 10 μm (C). Scale bar, 5 μm. (**D**) 3D FDTD simulation of the SPP intensity along the propagation direction. (**E**) Output characteristics of S1, S2, and S3 with V_{bias} = 7 V on the sources. (**F**) Photovoltage of the cascading detector and SPP source current versus propagation length. (**G**) Output characteristics of S2 under different voltage biases applied on the source. (**H**) Detector photovoltage and source current versus the voltage bias applied on the source.

length. Notably, the PV nature of the PIC system enabled the SPP energy to effectively transform into electricity without additional power consumption (*3*, *38*). By using the output characteristics of S1, S2, and S3, we calculated the experimental waveguide propagation loss α as (*38*)

$$\alpha = \frac{10}{z} \lg \frac{P_i}{P_o} \text{ (dB/cm)}$$

where z is the propagation length, P_i is the input energy, and P_o is the output energy. The short-circuit currents of S1, S2, and S3 were I_1 = 3.75×10^{-11} A, I_2 = 2.91×10^{-12} A, and I_3 = 3.47×10^{-13} A, respectively (Fig. 4E). Therefore, we experimentally obtained an averaged propagation loss of α = 2.29×10^4 dB cm^{-1} (more analyses are given in section S13). The calculated loss coefficient of the Au-strip waveguide using the 3D FDTD simulation was 3.83×10^3 dB cm^{-1}. The experimental propagation loss is approximately five times larger than that calculated by the FDTD simulation, which is attributed to the imperfections of the fabricated Au-strip waveguide (*39*). The experimental propagation loss is similar to that reported by van Wijngaarden *et al.* (*39*), indicating that the introduction of CNT-based active devices does not cause additional scatterings or imperfections.

After the SPP wave reaches the terminal of the waveguide, it enters the detector without noteworthy reflection by virtue of the ultrathin-diameter CNTs. The corresponding detection mechanism can be regarded as a multistep process: (i) The SPP energy is absorbed in the detector, generating electron-hole pairs via near-field coupling. (ii) The built-in field across the active CNT channel of the cascading detector separates the electron-hole pairs into free carriers before recombination. (iii) The free carriers are swept into corresponding electrodes to constitute the external flowing current. In addition, the transmitted SPP energy at the terminal of the detector could be regarded as zero because we experimentally demonstrated that no light was detected by the far-field spectrometer (fig. S11; more analyses are shown in section S14). Therefore, the launched SPP power can be estimated, and we define the exit of the source as P_1 and the entrance of the detector as P_2 (as shown in fig. S12).

The SPPs propagating in the detector are dissipated by the CNT absorption and waveguide loss. By taking the CNT absorption into account, we calculated the propagation loss as ~4.21×10^3 dB cm^{-1} via 3D FDTD simulation (more analyses are shown in section S16), which is larger than that of the waveguide of ~3.83×10^3 dB cm^{-1} without the CNTs. Therefore, the loss resulting from CNT absorption was calculated as 383.5 dB cm^{-1}. If a single-layer CNT film is assumed to have an absorption efficiency of ~3% (*28*, *40*), the energy required to generate 8 mV of photovoltage (fig. S13) is experimentally determined as ~1.374×10^{-10} W under normal incident illumination. Therefore, the ingoing power at P_2 was determined to be 8.34×10^{-9} W. Thus, the launched power for S3 was calculated as 1.21×10^{-7} W, enabling an estimation of the conversion efficiency between electricity and SPPs (more analyses are given in section S16). As shown in Fig. 4F, the flowing currents of these three SPP sources were approximately 1 mA, indicating that the stimulated electrical powers were approximately 7 mW in these three systems. Therefore, the conversion efficiency of S3 was approximately 1.72×10^{-5}, which is comparable to most of the previously reported CNT EL efficiencies (*9*, *25*). The conversion efficiency could be readily improved by aligning the CNT orientation along the waveguide direction to increase the coupled SPP energy (more analyses are given in section S18 and fig. S14).

The PIC system can potentially be used as a repeater for data transport in modern computing systems because of its electrically driven characteristic and PV operation mode (*3*). As evident in Fig. 4 (G and H), the photovoltage of S2 increased from 8 to 24 mV as the driving current was increased from 1.24×10^{-4} A (V_{bias} = 5 V) to 9.08×10^{-4} A (V_{bias} = 7 V). This result indicates that the energy could be readily tuned from electricity into SPPs at the source and efficiently transformed from the SPP domain into an electrical signal via the on-chip PV effect (*11*). In

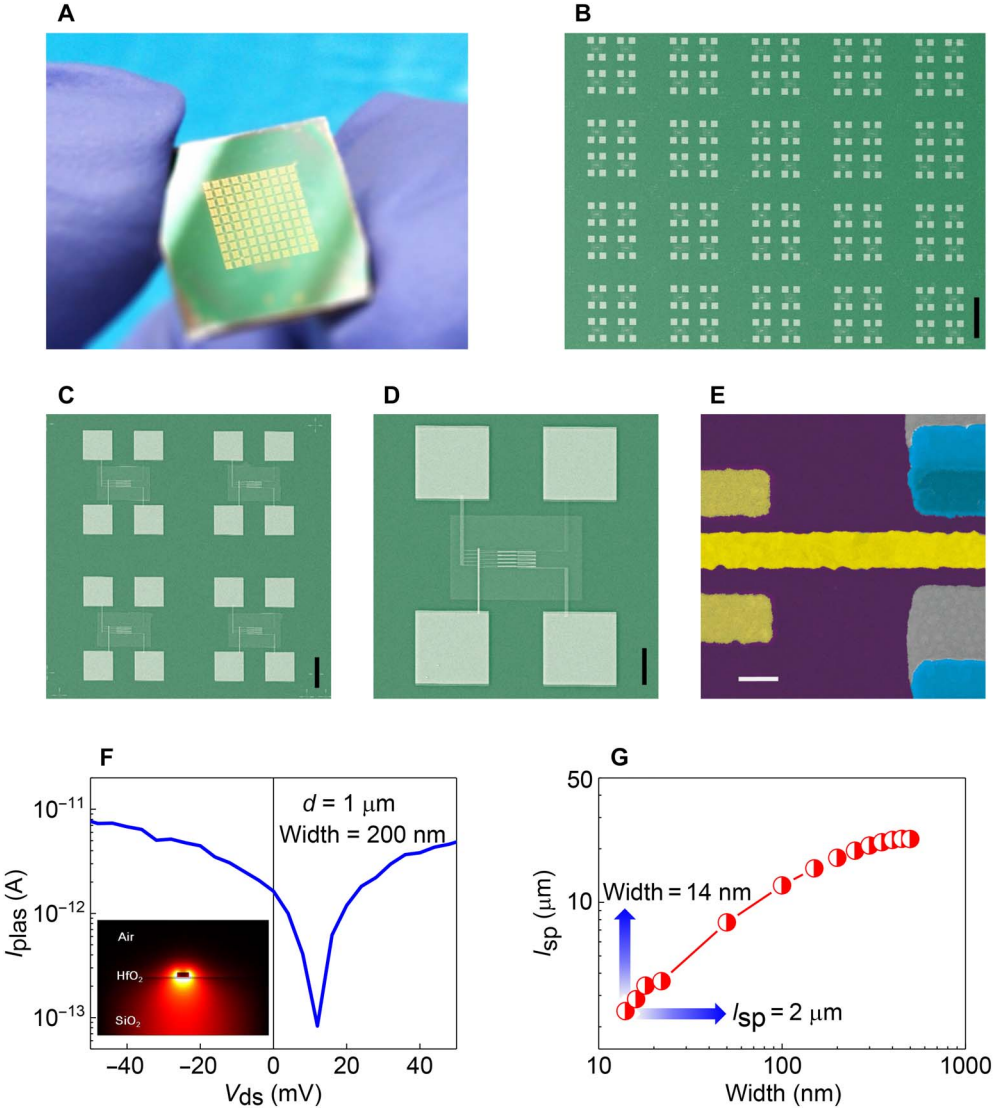

Fig. 5. Chip-level integration and deep-subwavelength characteristics. (**A**) Digital image of the PIC repeater array (wafer size, 10 mm × 10 mm). (**B** to **D**) SEM images of the repeater array (A) with different magnification levels. Scale bars in (B) to (D) are 250, 40, and 20 μm, respectively. (**E**) False-color SEM image of one channel in the PIC. Scale bar, 200 nm. (**F**) Output characteristics of the PIC. The inset shows the SPP mode distribution of the 200-nm-wide Au-strip waveguide. (**G**) SPP propagation length versus waveguide width.

principle, the recovered electricity could be fed back to drive subsequent signal processing circuits (*3*). Current electrically driven CNT emitters enable an extremely high emission speed of ~140 ps (*41*), and the response speed of CNT detectors is on the order of picoseconds (*42*). In principle, the introduction of the SPP structure will not significantly affect the speed of active CNT devices. Therefore, gigahertz-modulated PICs are reasonably expected to be realized in the future through utilization of the SPP source and detector in an extremely compact architecture (*11*).

DISCUSSION

The roadmap toward commercial utilization of PICs, such as repeaters in modern computing systems, requires realization of enhanced throughput capability and benchmarking feature size via currently mature CMOS-compatible methods (*2*, *11*–*13*). This objective can be readily achieved via the doping-free technique (*26*). As shown in Fig. 5A, we demonstrated the structural scalability of the PIC by fabricating a 20 × 20 PIC repeater array on a 10 mm × 10 mm chip, where the bottom-up CNT assembly and top-down device fabrication were seamlessly combined in a CMOS-compatible manner. Figure 5 (B to D) presents digital images of this array at different magnification levels, indicating that wafer-scale yield could be readily achieved via this doping-free method. In particular, no structural defects were observed under random SEM inspection over the entire chip. Such high uniformity and scalability are critical for large-scale applications.

In addition to the impressive throughput capability, the deep-subwavelength feature sizes were also realized via the doping-free technique. As shown in Fig. 5E, one channel of the PIC repeater was scaled to 200 nm, which exceeds the diffraction limit and approaches the deep-subwavelength scale (~λ/7, λ = 1340 nm). Meanwhile, the narrow waveguide also tightly confined the SPP mode distribution mainly below the Au strip to ensure the proper operation of the PIC (Fig. 5F, inset). Therefore, this miniaturized system could generate a photovoltage signal of 12 mV at the detector end (Fig. 5F). The propagation loss would substantially increase with further reduction of the width of the Au-strip waveguide. If we stipulate that the minimum propagation length of the SPPs is 2 μm for the PIC (Fig. 5G), the width of the Au-strip waveguide can be scaled to 14 nm (~λ/95, λ = 1340 nm), a size comparable to the microelectronic 14-nm technique node. Thus far, the contact width of a CNT device has been scaled to the sub–10-nm range (*29*, *30*), indicating that the pitch size of the PIC channel can be reduced to sub-30 nm in principle. To the best of our knowledge, this work represents the first report of a monolithic subwavelength-scaled PIC system, demonstrating the synergy of plasmonic, electronic, and photonic components to realize complete, large-scale PICs.

CONCLUSION

We demonstrated a monolithic subwavelength electrically driven PIC system consisting of electrically tunable SPP sources, a PV cascading SPP detector, and Au-strip waveguides. These components were fabricated from CNTs of the same feature size via a CMOS-compatible doping-free technique, providing an ideal platform for the realization of deep-subwavelength (~λ/7 to λ/95, λ = 1340 nm) and large-scale (20 × 20 PIC array) plasmonic circuits. The circuits were configured as repeaters by virtue of their electrically driven characteristics and PV operation mode to freely transform between SPPs and electrical signals. CNTs offer an excellent material system for combining plasmonics with CNT-based nano- or optoelectronic functional devices, opening a new path for a monolithic, deep-subwavelength, photonic-electronic integrated system that may reform the architecture of currently computing paradigms by adding nanophotonics as a new design dimension.

MATERIALS AND METHODS

Fabrication of the PIC system

The PIC systems were fabricated on a typical silicon wafer with 500-nm SiO_2. The electrodes of SPP sources (titanium/gold, 5/40 nm) were fabricated via electron beam lithography (EBL) (Raith150 Two), electron beam evaporation (EBE) (Kurt J. Lesker), and standard lift-off process. The electrodes and virtual contacts of the detectors (scandium, 80 nm; palladium, 70 nm) were fabricated with the same procedure as that of the SPP sources. CNTs outside the active channels were etched using reactive ion etching (Trion Minilock-Phantom III). The HfO_2 layer was deposited via low-temperature atomic layer deposition (Cambridge Nanotech). The Au-strip waveguides were fabricated using the same EBL, EBE, and lift-off process.

Device characterization

The detector was characterized by supercontinuum spectrum laser (NKT Company). Optoelectronic measurements on CNT devices were performed with a probe station (Märzhäuser Wetzlar GmbH & Co. KG) attached to the Horiba system (Jobin Yvon/Horiba Company). All electronic transportation measurements were performed with a Keithley 4200 semiconductor analyzer at room temperature under ambient conditions. PL, EL, and Raman spectra were characterized on the Horiba platform. Excitation wavelength was 633 nm for the Raman and PL characterization. The noise spectrum was obtained with Agilent B1500 under ambient conditions.

Numerical simulation

Simulations were carried out via FDTD Solutions version 8.0 (Lumerical Inc.).

SUPPLEMENTARY MATERIALS

Supplementary material for this article is available at http://advances.sciencemag.org/cgi/content/full/3/10/e1701456/DC1

section S1. Definition of the device parameter
section S2. Preparation and characterization of (8, 4) and (8, 3) and high-semiconducting-purity CNTs
section S3. Analysis of the Au-strip waveguide mode
section S4. PL spectra of the nonchirality-selected and (8, 4) and (8, 3) CNTs
section S5. PL and EL spectra of the (8, 4) and (8, 3) CNTs-based emitter
section S6. Propagation loss of the Au-strip waveguide versus vacuum wavelength
section S7. Analysis of the FWHM of the SPP source
section S8. Far-field emission of the LSPs
section S9. Structure and performance of the CNT-based PV cascading detector
section S10. The reason to select cascading SPP detector
section S11. The near-field enhancement of the Au-strip waveguide
section S12. Three-dimensional FDTD calculation of the SPP waveguide mode
section S13. Calculation of the experimental propagation loss
section S14. Analysis of the transmitted SPP energy in the detector
section S15. SEM image of S3 indicating the exit of the source as P1 and the entrance the detector as P2
section S16. Calculation of the conversion efficiency
section S17. Estimation of the power to generate 8 mV photovoltage
section S18. Analysis of the coupling efficiency as a function of CNT orientation versus Au-strip waveguide
fig. S1. Definition of the channel length and width in the PIC system.
fig. S2. Raman spectra of (8, 4) and (8, 3) and high–semiconducting purity CNTs.
fig. S3. Mode distribution of the Au-strip waveguide.
fig. S4. PL spectra.

fig. S5. PL and EL spectra of the (8, 4) and (8, 3) CNT-based emitter.
fig. S6. Propagation loss of the Au-strip waveguide versus vacuum wavelength.
fig. S7. Analysis of the LSPs induced far-field emission.
fig. S8. Structure and performance of the CNT cascading detector.
fig. S9. Characteristics of the single-channel PIC.
fig. S10. Near-field enhancement of the Au-strip waveguide.
fig. S11. EL spectrum collected at the end of the detector.
fig. S12. SEM image of S3 indicating the exit of the source as P_1 and the entrance of the detector as P_2.
fig. S13. Photoresponse of the cascading detector under normal incident IR illumination.
fig. S14. Schematic of the CNT orientation versus Au-strip waveguide direction.
table S1. Averaged diameter, bandgap, and absorption range of (8, 4) and (8, 3) and high–semiconducting purity CNTs.
References (*43*–*45*)

REFERENCES AND NOTES

1. M. M. Waldrop, The chips are down for Moore's law. *Nature* **530**, 144–147 (2016).
2. R. Kirchain, L. Kimerling, A roadmap for nanophotonics. *Nat. Photonics* **1**, 303–305 (2007).
3. P. Bhattacharya, *Semiconductor Optoelectronic Devices* (Prentice-Hall, 1994).
4. C. Sun, M. T. Wade, Y. Lee, J. S. Orcutt, L. Alloatti, M. S. Georgas, A. S. Waterman, J. M. Shainline, R. R. Avizienis, S. Lin, B. R. Moss, R. Kumar, F. Pavanello, A. H. Atabaki, H. M. Cook, A. J. Ou, J. C. Leu, Y.-H. Chen, K. Asanović, R. J. Ram, M. A. Popović, V. M. Stojanović, Single-chip microprocessor that communicates directly using light. *Nature* **528**, 534–538 (2015).
5. P. Chaisakul, D. Marris-Morini, J. Frigerio, D. Chrastina, M.-S. Rouifed, S. Cecchi, P. Crozat, G. Isella, L. Vivien, Integrated germanium optical interconnects on silicon substrates. *Nat. Photonics* **8**, 482–488 (2014).
6. P. J. Pauzauskie, P. Yang, Nanowire photonics. *Mater. Today* **9**, 36–45 (2006).
7. F. H. L. Koppens, T. Mueller, Ph. Avouris, A. C. Ferrari, M. S. Vitiello, M. Polini, Photodetectors based on graphene, other two-dimensional materials and hybrid systems. *Nat. Nanotechnol.* **9**, 780–793 (2014).
8. M. Paniccia, Integrating silicon photonics. *Nat. Photonics* **4**, 498–499 (2010).
9. S. Khasminskaya, F. Pyatkov, K. Słowik, S. Ferrari, O. Kahl, V. Kovalyuk, P. Rath, A. Vetter, F. Hennrich, M. M. Kappes, G. Gol'tsman, A. Korneev, C. Rockstuhl, R. Krupke, W. H. P. Pernice, Fully integrated quantum photonic circuit with an electrically driven light source. *Nat. Photonics* **10**, 727–732 (2016).
10. E. Ozbay, Plasmonics: Merging photonics and electronics at nanoscale dimensions. *Science* **311**, 189–193 (2006).
11. V. J. Sorger, R. F. Oulton, R.-M. Ma, X. Zhang, Toward integrated plasmonic circuits. *MRS Bull.* **37**, 728–738 (2012).
12. T. W. Ebbesen, C. Genet, S. I. Bozhevolnyi, Surface-plasmon circuitry. *Phys. Today* **61**, 44–50 (2008).
13. W. L. Barnes, A. Dereux, T. W. Ebbesen, Surface plasmon subwavelength optics. *Nature* **424**, 824–830 (2003).
14. E. Verhagen, M. Spasenović, A. Polman, L. K. Kuipers, Nanowire plasmon excitation by adiabatic mode transformation. *Phys. Rev. Lett.* **102**, 203904 (2009).
15. Y. Liu, S. Palomba, Y. Park, T. Zentgraf, X. Yin, X. Zhang, Compact magnetic antennas for directional excitation of surface plasmons. *Nano Lett.* **12**, 4853–4858 2012).
16. J. A. Dionne, K. Diest, L. A. Sweatlock, H. A. Atwater, PlasMOStor: A metal–oxide–Si field effect plasmonic modulator. *Nano Lett.* **9**, 897–902 2009).
17. J. S. Q. Liu, R. A. Pala, F. Afshinmanesh, W. Cai, M. L. Brongersma, A submicron plasmonic dichroic splitter. *Nat. Commun.* **2**, 525 2011).
18. A. Drezet, D. Koller, A. Hohenau, A. Leitner, F. R. Aussenegg, J. R. Krenn, Plasmonic crystal demultiplexer and multiports. *Nano Lett.* **7**, 1697–1700 (2007).
19. W. Du, T. Wang, H.-S. Chu, L. Wu, R. Liu, S. Sun, W. K. Phua, L. Wang, N. Tomczak, C. A. Nijhuis, A On-chip molecular electronic plasmon sources based on self-assembled monolayer tunnel junctions. *Nat. Photonics* **10**, 274–280 (2016).
20. P. Neutens, P. Van Dorpe, I. De Vlaminck, L. Lagae, G. Borghs, Electrical detection of confined gap plasmons in metal–insulator–metal waveguides. *Nat. Photonics* **3**, 283–286 (2009).
21. P. Rai, N. Hartmann, J. Berthelot, J. Arocas, G. C. des Francs, A. Hartschuh, A. Bouhelier, Electrical excitation of surface plasmons by an individual carbon nanotube transistor. *Phys. Rev. Lett.* **111**, 026804 (2013).
22. R. J. Walters, R. V. A. van Loon, I. Brunets, J. Schmitz, A. Polman, A silicon-based electrical source of surface plasmon polaritons. *Nat. Mater.* **9**, 21–25 (2010).
23. D. Pacifici, H. J. Lezec, H. A. Atwater, All-optical modulation by plasmonic excitation of CdSe quantum dots. *Nat. Photonics* **1**, 402–406 (2007).
24. A. L. Falk, F. H. L. Koppens, L. Y. Chun, K. Kang, N. de Leon Snapp, A. V. Akimov, M.-H. Jo, M. D. Lukin, H. Park, Near-field electrical detection of optical plasmons and single-plasmon sources. *Nat. Phys.* **5**, 475–479 (2009).
25. P. Avouris, M. Freitag, V. Perebeinos, Carbon-nanotube photonics and optoelectronics. *Nat. Photonics* **2**, 341–350 (2008).
26. L.-M. Peng, Z. Zhang, S. Wang, Carbon nanotube electronics: Recent advances. *Mater. Today* **17**, 433–442 (2014).
27. S. Wang,Q. Zeng, L. Yang, Z. Zhang, Z. Wang, T. Pei, L. Ding, X. Liang, M. Gao,Y. Li, L.-M. Peng, High-performance carbon nanotube light-emitting diodes with asymmetric contacts. *Nano Lett.* **11**, 23–29 (2011).
28. Y. Liu, N. Wei, Q. Zeng, J. Han, H. Huang, D. Zhong, F. Wang, L. Ding, J. Xia, H. Xu, Z. Ma, S. Qiu, Q. Li, X. Liang, Z. Zhang, S. Wang, L.-M. Peng, Room temperature broadband infrared carbon nanotube photodetector with high detectivity and stability. *Adv. Opt. Mater.* **4**, 238–245 (2016).
29. A. D. Franklin, Z. Chen, Length scaling of carbon nanotube transistors. *Nat. Nanotechnol.* **5**, 858–862 (2010).
30. H. Xu, S. Wang, Z. Zhang, L.-M. Peng, Length scaling of carbon nanotube electric and photo diodes down to sub-50 nm. *Nano Lett.* **14**, 5382–5389 (2014).
31. Q. Cao, S.-J. Han, J. Tersoff, A. D. Franklin, Y. Zhu, Z. Zhang, G. S. Tulevski, J. Tang, W. Haensch, End-bonded contacts for carbon nanotube transistors with low, size-independent resistance. *Science* **350**, 68–72 (2015).
32. L. Yang, S. Wang, Q. Zeng, Z. Zhang, T. Pei, Y. Li, L.-M. Peng, Efficient photovoltage multiplication in carbon nanotubes. *Nat. Photonics* **5**, 672–676 (2011).
33. M. M. Shulaker, G. Hills, N. Patil, H. Wei, H.-Y. Chen, H.-S. P. Wong, S. Mitra, Carbon nanotube computer. *Nature* **501**, 526–530 (2013).
34. M. E. Itkis, A. Yu, R. C. Haddon, Single-walled carbon nanotube thin film emitter-detector integrated optoelectronic device. *Nano Lett.* **8**, 2224–2228 (2008).
35. J. Chen, V. Perebeinos, M. Freitag, J. Tsang, Q. Fu, J. Liu, P. Avouris, Bright infrared emission from electrically induced excitons in carbon nanotubes. *Science* **310**, 1171–1174 (2005).
36. S. Liang, Z. Ma, N. Wei, H. Liu, S. Wang, L.-M. Peng, Solid state carbon nanotube device for controllable trion electroluminescence emission. *Nanoscale* **8**, 6761–6769 (2016).
37. V. Perebeinos, J. Tersoff, P. Avouris, Scaling of excitons in carbon nanotubes. *Phys. Rev. Lett.* **92**, 257402 (2004).
38. B. E. Saleh, M. C. Teich, B. E. Saleh, *Fundamentals of Photonics* (Wiley, 1991).
39. J. T. van Wijngaarden, E. Verhagen, A. Polman, C. E. Ross, H. J. Lezec, H. A. Atwater, Direct imaging of propagation and damping of near-resonance surface plasmon polaritons using cathodoluminescence spectroscopy. *Appl. Phys. Lett.* **88**, 221111 (2006).
40. M. E. Itkis, F. Borondics, A. Yu, R. C. Haddon, Bolometric infrared photoresponse of suspended single-walled carbon nanotube films. *Science* **312**, 413–416 (2006).
41. T. Mori, Y. Yamauchi, S. Honda, H. Maki, An electrically driven, ultrahigh-speed, on-chip light emitter based on carbon nanotubes. *Nano Lett.* **14**, 3277–3283 (2014).
42. L. Prechtel, L. Song, S. Manus, D. Schuh, W. Wegscheider, A. W. Holleitner, Time-resolved picosecond photocurrents in contacted carbon nanotubes. *Nano Lett.* **11**, 269–272 (2010).
43. H. Liu, D. Nishide, T. Tanaka, H. Kataura, Large-scale single-chirality separation of single-wall carbon nanotubes by simple gel chromatography. *Nat. Commun.* **2**, 309 (2011).
44. R. Krupke, F. Hennrich, H. v. Löhneysen, M. M. Kappes, Separation of metallic from semiconducting single-walled carbon nanotubes. *Science* **301**, 344–347 (2003).
45. M. S. Dresselhaus, G. Dresselhaus, R. Saito, A. Jorio, Raman spectroscopy of carbon nanotubes. *Phys. Rep.* **409**, 47–99 (2005).

Acknowledgments

Funding: This work was financially supported by the Ministry of Science and Technology of China (grant no. 2016YFA0201901) and the National Natural Science Foundation of China (grant nos. 61377050, 11574011, 61370009, and 11634014). **Author contributions:** L.-M.P. supervised the project. Y.L. conceived the study, fabricated devices, and performed all electronic and optoelectronic measurements. Y.L. and J.Z. performed the corresponding numerical simulations and co-analyzed the data. H.L. performed separation and processing of (8, 4)- and (8, 3)-enriched CNTs. Y.L., J.Z., and L.-M.P. wrote the article. L.-M.P. and S.W. built research infrastructures. All authors contributed significant discussion of the data. **Competing interests:** The authors declare that they have no competing interests. **Data and materials availability:** All data needed to evaluate the conclusions in the paper are present in the paper and/or the Supplementary Materials. Additional data related to this paper may be requested from the authors.

Submitted 4 May 2017
Accepted 28 September 2017
Published 20 October 2017
10.1126/sciadv.1701456

Citation: Y. Liu, J. Zhang, H. Liu, S. Wang, L.-M. Peng, Electrically driven monolithic subwavelength plasmonic interconnect circuits. *Sci. Adv.* **3**, e1701456 (2017).